

Data-Driven Reconstruction of Significant Wave Heights from Sparse Observations

Hongyuan Shi^{a,b}, Yilin Zhai^{a,*}, Ping Dong^a, Zaijin You^{a,c}, Chao Zhan^{a,b},
Qing Wang^{a,b}

^a*School of Hydraulic and Civil Engineering, Ludong University, Shandong, 264025, Yantai, China*

^b*Institute of Coastal Research, Ludong University, Yantai, 264025, Shandong, China*

^c*Navigation College, Dalian Maritime University, Dalian, 116026, Liaoning, China*

Abstract

Reconstructing high-resolution regional significant wave height fields from sparse and uneven buoy observations remains a core challenge for ocean monitoring and risk-aware operations. We introduce AUWave, a hybrid deep learning framework that fuses a station-wise sequence encoder (MLP) with a multi-scale U-Net enhanced by a bottleneck self-attention layer to recover 32×32 regional SWH fields. A systematic Bayesian hyperparameter search with Optuna identifies the learning rate as the dominant driver of generalization, followed by the scheduler decay and the latent dimension. Using NDBC buoy observations and ERA5 reanalysis over the Hawaii region, AUWave attains a minimum validation loss of 0.043285 and a slightly right-skewed RMSE distribution. Spatial errors are lowest near observation sites and increase with distance, reflecting identifiability limits under sparse sampling. Sensitivity experiments show that AUWave consistently outperforms a representative baseline in data-richer configurations, while the baseline is only marginally competitive in the most underdetermined single-buoy cases. The architecture’s multi-scale and attention components translate into accuracy gains when minimal but non-trivial spatial anchoring is available. Error maps and buoy ablations reveal key anchor stations whose removal disproportionately degrades performance, offering actionable guidance for network design. AUWave provides a scalable pathway for gap filling, high-resolution priors for data assimilation, and contingency reconstruction.

*Corresponding author

Keywords: Significant Wave Height, Sparse Observations, Deep Learning, U-Net, Attention

1. Introduction

Significant wave height (SWH) underpins maritime safety, coastal engineering, renewable energy siting, and climate applications (Caloiero et al., 2022; Gao et al., 2023; Shi et al., 2023). Accurate knowledge of SWH is essential for navigation risk assessment, offshore structure design, and wave energy harvesting, as well as for understanding long-term ocean–atmosphere interactions and their role in climate variability (Hajinezhadian and Behnam, 2023; Patra et al., 2024; Seo et al., 2023; Azman et al., 2021; Zhang et al., 2025; Ibarra-Berastegui et al., 2023).

However, operational observations remain sparse and heterogeneous: in-situ buoy networks provide highly accurate but pointwise and irregular measurements, often constrained to coastal or shipping routes, while satellite altimeters can provide broad coverage for ocean measurements, their sampling is primarily limited to the satellite’s trajectory in both time and space, and the revisit delay for a specific location can be relatively long (Le Traon et al., 2025). Reanalysis products and global hindcasts provide spatially continuous fields, yet these are generated by numerical models that may contain systematic errors or biases, especially in regions with limited assimilated data (Wang and Wang, 2022; Riley, 2023, 2024). Bridging this scale and sampling gap to reconstruct high-resolution regional wave fields from limited observations is therefore both practically relevant and scientifically challenging, with direct implications for both operational forecasting and scientific understanding.

Classical mapping methods—such as interpolation and data assimilation—attempt to fill this observational gap, but they rely on assumed covariance structures and tend to degrade when observations are scarce, unevenly distributed, or located far from dynamically active regions (Asch et al., 2016; Fletcher, 2017). Physics-based spectral wave models, on the other hand, yield dynamically consistent fields and can simulate the evolution of wave spectra across large spatial and temporal scales. Yet they are dependent on accurate external forcing (e.g., high-quality wind fields), careful calibration of parameterizations, and substantial computational resources for both real-time forecasting and long-term hindcasts (Gaffet et al., 2025; Yao et al.,

2025). These constraints limit their practical deployment in regional, high-resolution applications where fast updates and robustness to sparse data are required.

In recent years, deep learning approaches have emerged as promising alternatives: by learning complex mappings directly from data, they offer the potential to bypass explicit assumptions of covariance or dynamics and instead exploit statistical regularities from large training datasets. In geosciences, neural networks have demonstrated success in tasks such as image-to-image translation, super-resolution, and geophysical field reconstruction, indicating their capability to extract both local and global patterns beyond what classical methods can achieve (Huang et al., 2024; Ijeh et al., 2023; Song and Alkhalifah, 2021).

Several deep learning approaches for wave reconstruction have been explored. (Han et al., 2023) proposed DGWBNet, which employs conditional variational autoencoders and adversarial learning to achieve joint estimation of SWH, period, and direction, while also providing uncertainty quantification. (Duan et al., 2024) developed the RWR model, utilizing fully connected and convolutional neural networks to reconstruct regional SWH and analyzing the impact of spatial boundaries and the number of buoys on accuracy. (Lv et al., 2025) integrated U-Net and GAN within an Actor-Critic framework to simultaneously achieve optimal observation point selection and multidimensional wave field reconstruction.

While these methods have advanced wave field reconstruction, they also exhibit certain limitations: generative approaches (DGWBNet) and co-optimization frameworks (Actor-Critic) often entail high training complexity and computational burden, which may not be necessary for deterministic reconstruction tasks. In contrast, more straightforward feedforward designs, though computationally efficient, struggle to capture the non-local spatial dependencies of wave propagation due to the excessive reliance of standard convolutions on local patterns. Furthermore, sensor layout optimization frameworks are often difficult to apply in common practical scenarios.

Addressing these limitations, this paper proposes the AUWave model, which combines multilayer perceptron and U-Net architectures to better capture both local and global features under fixed observation point layouts and single-parameter settings, thereby improving reconstruction accuracy. Additionally, this study introduces, for the first time, automated hyperparameter and architectural optimization using Optuna, systematically exploring model configurations to significantly enhance accuracy and stability while reducing

reliance on manual design based on empirical experience.

The main contributions of this paper are as follows:

- A novel network architecture is proposed, which effectively integrates Multilayer Perceptron (MLP) with U-Net. This design preserves the convolutional structure’s ability to capture local features while compensating for the shortcomings in modeling non-local dependencies through MLP.
- Automated hyperparameter and architectural optimization is introduced. For the first time in wave field reconstruction tasks, the Optuna framework is employed to systematically search for optimal network hyperparameters and structural configurations, overcoming the limitations of manual tuning.
- Improved reconstruction accuracy and stability are achieved. Under identical data and observation conditions, AUWave significantly outperforms existing methods, demonstrating its effectiveness and generalizability in sparse observation scenarios.

The remainder of the paper is organized as follows. Section 2 describes the study area, data, preprocessing, model architecture, and hyperparameter optimization. Section 3 presents ablation studies, spatial-temporal error analyses, and buoy-configuration sensitivity, with comparisons to the RWR baseline. Section 4 discusses implications, limitations, and future directions. Section 5 concludes.

2. Methods

2.1. Study Area and Data

The dataset used for model training and evaluation comprises SWH measurements obtained from two primary sources: (1) sparse in-situ observations provided by the National Data Buoy Center (NDBC), and (2) gridded field data (32×32) derived from the ERA5 reanalysis product. The ERA5 dataset offers a spatial resolution of 0.5° and a temporal resolution of 1 hour, ensuring consistency across study regions and enabling robust model evaluation (see Figure 1).

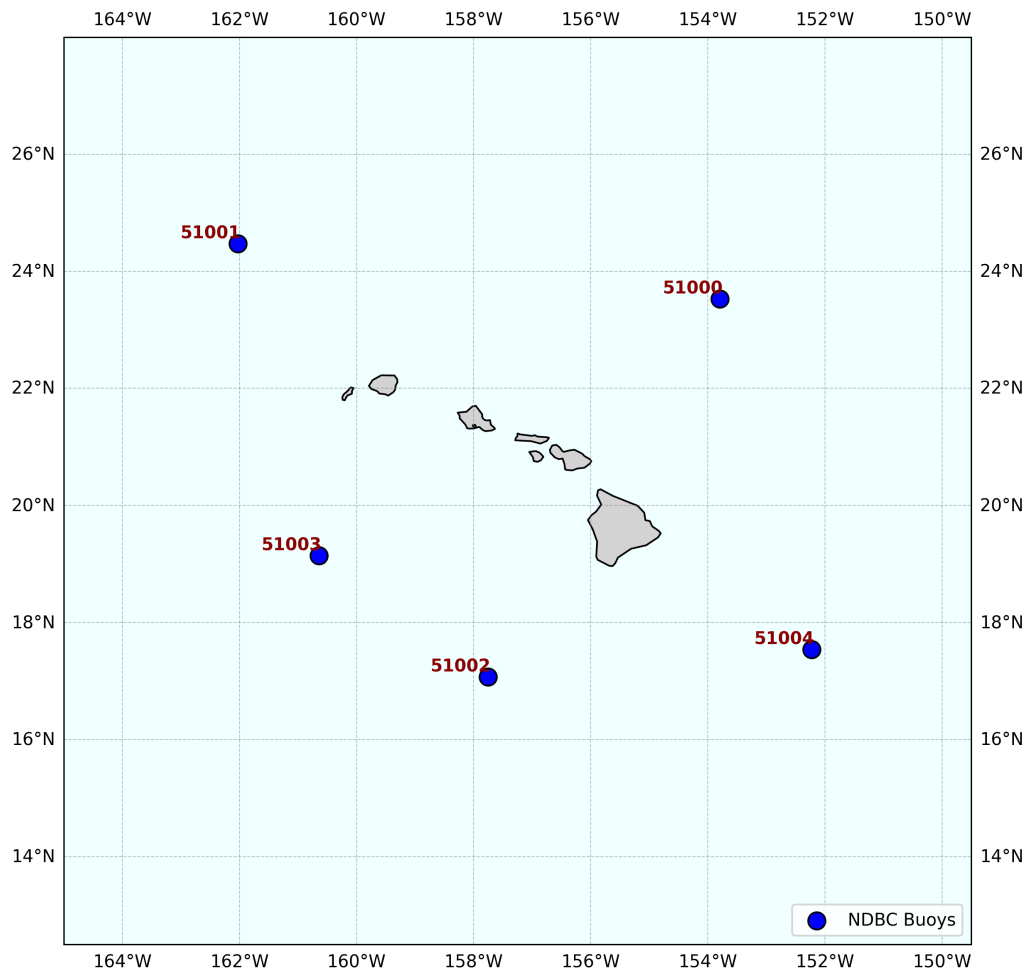


Figure 1: Study Area and Buoy Locations

2.2. Data Preprocessing

The raw NDBC buoy records span the period from 2022 to 2023. To ensure temporal consistency and spatial comparability between in-situ observations and ERA5 reanalysis, both datasets were systematically processed to enable direct comparison and joint analysis. First, quality-controlled buoy measurements were extracted from the National Data Buoy Center (NDBC), and records with missing SWH values were removed. Since reporting times across stations are not perfectly synchronized (e.g., observations at different minutes within an hour), all timestamps were rounded to the nearest full hour. Duplicate entries were subsequently aggregated by `[timestamp, station_id]`, retaining the first record.

ERA5 reanalysis data were simultaneously pre-processed to extract SWH values on a latitude-longitude grid. To align the two datasets, the intersection of timestamps common to both buoy records and ERA5 outputs was identified and used as the shared temporal index. Based on this unified time axis, ERA5 data were organized into a four-dimensional array with dimensions corresponding to `[time, variable, latitude, longitude]`, where each record was mapped to its grid cell according to the spatial indices of latitude and longitude. The buoy data were aligned to the same time index, forming a two-dimensional array with rows representing time steps and columns representing stations.

For strict temporal consistency, only time steps with complete buoy observations across all stations were retained. ERA5 data were chronologically sorted, and missing values in numerical fields were filled with zeros to mitigate sparsity.

Finally, the aligned dataset was split in chronological order: the first 70% of samples were used as the training set, the middle 15% as the testing set for hyperparameter tuning and model architecture search, and the final 15% as the validation set for independent performance evaluation.

2.3. AUWave Model Architecture

To reconstruct 2D wave fields from sparse time series, we develop a deep learning model named AUWave (see Figure 2), which integrates a MLP, a U-Net encoder-decoder, and self-attention mechanisms. The model is implemented using PyTorch and PyTorch Lightning frameworks. It takes as input a sparse wave sequence represented by a one-dimensional vector of size $1 \times n$, where n denotes the total number of buoy stations in the study region and

each entry corresponds to the SWH at a given station and time. The model outputs a 32×32 single-channel wave field grid.

The MLP module consists of three fully connected layers with hidden dimensions [896, 832, 800], projecting the input into a 1792-dimensional latent space. Batch normalization and LeakyReLU activation (slope = 0.2) are applied at each layer. A linear projection then reshapes the encoded vector into an initial 2D wave field of size $1 \times 32 \times 32$ (Xu et al., 2020).

The core network adopts a canonical U-Net-like architecture featuring a symmetric encoder-decoder topology with five hierarchical downsampling and upsampling stages. This configuration enables progressive abstraction of spatial information during encoding and faithful reconstruction of high-resolution outputs during decoding. The encoder channel widths are defined as [64, 64, 64, 64, 2688], gradually increasing representational capacity while reducing spatial resolution, whereas the decoder mirrors this configuration with [2688, 64, 64, 64, 64], facilitating the recovery of fine-scale features through successive upsampling (He et al., 2016).

Each stage is composed of three residual blocks based on the ResNet paradigm, which are known to alleviate vanishing gradient issues and allow for efficient training of deeper networks. Within each residual block, 3×3 convolutional filters are employed to capture local spatial correlations, followed by group normalization with 32 groups to stabilize feature distributions and improve generalization across varying batch sizes. The SiLU (Sigmoid Linear Unit) activation function is subsequently applied, offering smooth, non-monotonic nonlinearity that improves optimization dynamics compared to ReLU-like activations (He et al., 2020; Wu, 2022; Ramachandran et al., 2017).

To enhance global context modeling, a self-attention mechanism is incorporated at the U-Net bottleneck (Vaswani et al., 2023).

The model is trained using the mean squared error (MSE) loss. To ensure numerical stability and improve model training efficiency, all input and output data were transformed using a $\log(1+x)$ function. After prediction, the results were denormalized to recover the original wave height values. Key hyperparameters, such as hidden layer dimensions and learning rate, are optimized using the Optuna framework (see Section 2.4 for details).

$$\text{MSE} = \frac{1}{n} \sum_{i=1}^n (y_i - \hat{y}_i)^2 \quad (1)$$

were variable, and the possibility of incorporating attention mechanisms was also explored.

To balance exploration and exploitation, we adopted the Tree-structured Parzen Estimator (TPE) as the core sampling algorithm. TPE is a Bayesian optimization method that constructs probabilistic models from past trials to suggest promising hyperparameter sets. To further improve efficiency, we employed a Median Pruner, which compares the current trial’s loss with the median of completed trials at the same step. Trials performing significantly worse than the median were terminated early to focus computational resources on more promising configurations (Watanabe, 2023).

A total of 500 optimization trials were conducted. Each trial was trained for up to 100000 epochs, with early stopping enabled: if the validation loss did not improve within 100 consecutive epochs, the training was halted. After exhaustive tuning, we obtained the optimal hyperparameter combination, achieving a minimum validation loss of 0.043285. This configuration was adopted for all subsequent experiments and final model training.

Category	Hyperparameter	Search Space	Description
Optimizer	Learning Rate	$[10^{-5}, 10^{-3}]$	Controls the update step size of model parameters.
	Scheduler Gamma	$[0.9, 0.99]$	Decay factor for the StepLR scheduler.
MLP	Layers	$[1, 4]$	Number of layers in MLP
	Hidden Dimensions	$[128, 4096]$	Dimension of the fully connected layers in the sequence encoder.
	Latent Dimension	$[256, 2048]$	Dimension of the encoded features.
U-Net	Number of Blocks	$[3, 5]$	Number of down-sampling and up-sampling blocks.
	Layers per Block	$[1, 3]$	Number of convolutional layers within each U-Net block.
	Output Channels	$[32, 8192]$	Output channels for each block in the U-Net.
	Attention Mechanism	$[True, False]$	Enables the use of attention modules within the U-Net.

Table 1: Hyperparameter Search Space

3. Results

3.1. Ablation and Sensitivity Analysis

To better understand the influence of individual hyperparameters on the model’s performance, we visualize the optimization process and the parameter importance derived from 500 Optuna trials, as shown in Figure 3.

Figure 3(a) illustrates the objective value over trials. A clear downward trend is observed, demonstrating that the optimization converged effectively and consistently identified improved configurations over time. The best-performing configuration achieved a validation loss of 0.043285.

Figure 3(b) shows the relative importance of each hyperparameter based on Optuna’s internal model. The learning rate emerged as the most critical factor (~51% contribution), followed by the scheduler decay rate and latent dimension. Structural parameters such as U-Net depth or attention usage had relatively minor influence. These guided the final model configuration and further justify the use of automated hyperparameter tuning.

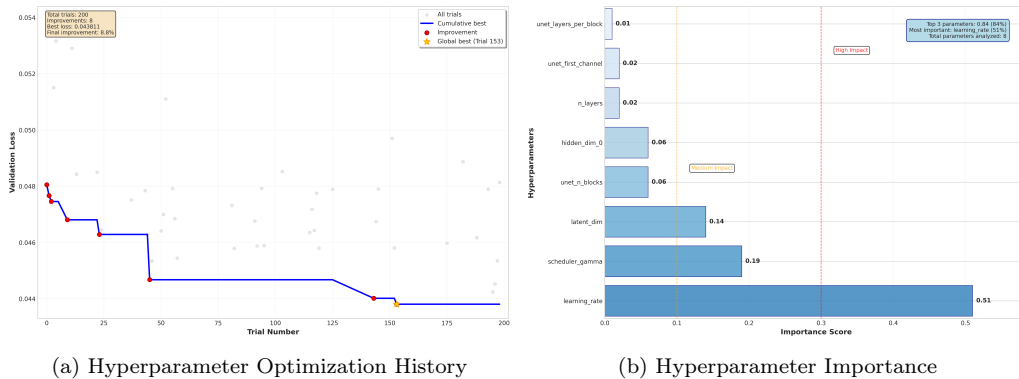


Figure 3: Hyperparameter optimization results using Optuna.

3.2. Temporal Variability of Reconstruction Errors

To visually assess the model’s performance, we compare the true and predicted wave fields for five randomly selected examples from the Hawaii dataset. Each example includes three subplots: (a) the true wave field, (b) the predicted wave field, and (c) the error map with the Root Mean Square Error (RMSE) value indicated in the title. The comparisons are presented in Figures 4 to 8. The locations of the sparse input buoys are marked with red crosses (‘x’), and land areas are masked in white.

These figures demonstrate the model is generally successful in capturing the main spatial characteristics of the ocean wave field. For instance, in cases with low overall error, such as the examples with RMSE values of 0.1463 and 0.1647 (Figure 8 and Figure 6c), the predicted field exhibits a high degree of similarity to the ground truth. The model accurately reproduces the location, shape, and magnitude of the primary wave amplitude crests and troughs.

Conversely, the figure also includes cases where the reconstruction is less accurate. The example with the highest error (RMSE = 0.3574, Figure 4c) demonstrates notable discrepancies. While the general large-scale pattern is still discernible, the error map reveals significant localized areas of both overestimation (red patches) and underestimation (dark blue patches). These larger errors predominantly occur in regions distant from the sparse buoy locations, underscoring the inherent challenge of interpolating complex oceanographic features over data-sparse areas. Intermediate cases, such as those with RMSE values of 0.2097 and 0.2183 (Figure 5c and Figure 7c), represent a typical level of performance, where the main wave structures are correctly identified but with some inaccuracies in amplitude and fine-scale details.

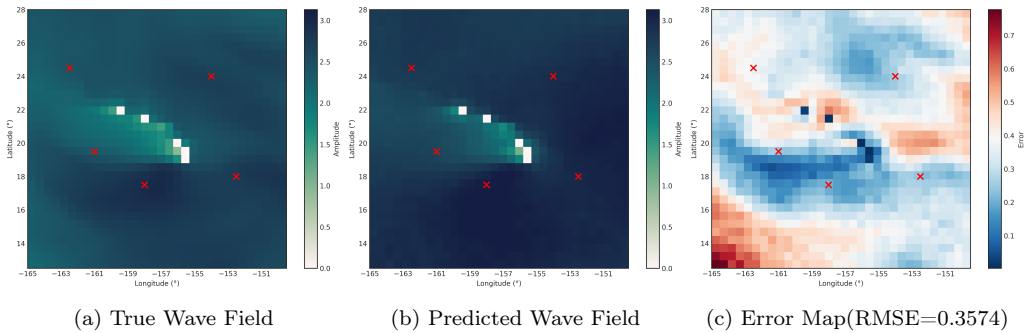


Figure 4: Comparison of true and predicted wave fields for Hawaii dataset (example 1).

3.3. RMSE Distribution and Spatial Patterns

In addition to individual examples, we analyze the overall RMSE distribution across the entire Hawaii dataset to understand the spatial and temporal error patterns. Figure 9 presents (a) the spatial distribution of RMSE values at each grid point, with warmer colors indicating higher errors, and (b) a histogram of RMSE values over all time steps, showing the frequency of different error magnitudes. This analysis helps identify areas and periods

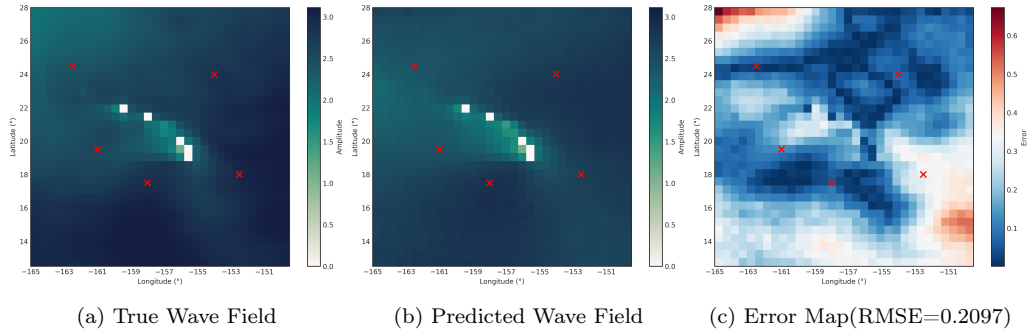


Figure 5: Comparison of true and predicted wave fields for Hawaii dataset (example 2).

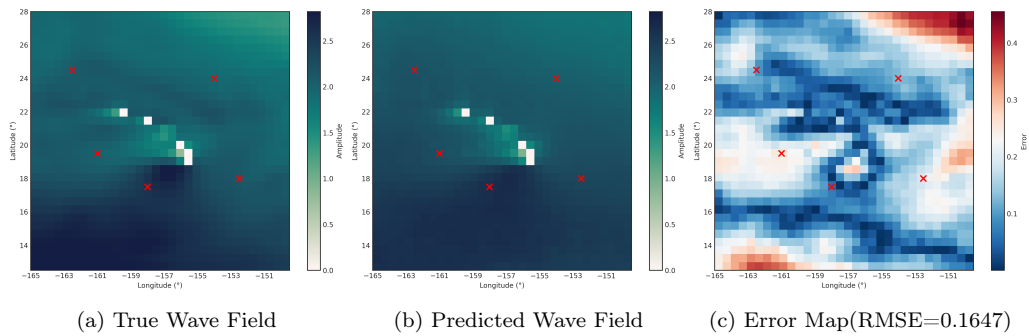


Figure 6: Comparison of true and predicted wave fields for Hawaii dataset (example 3).

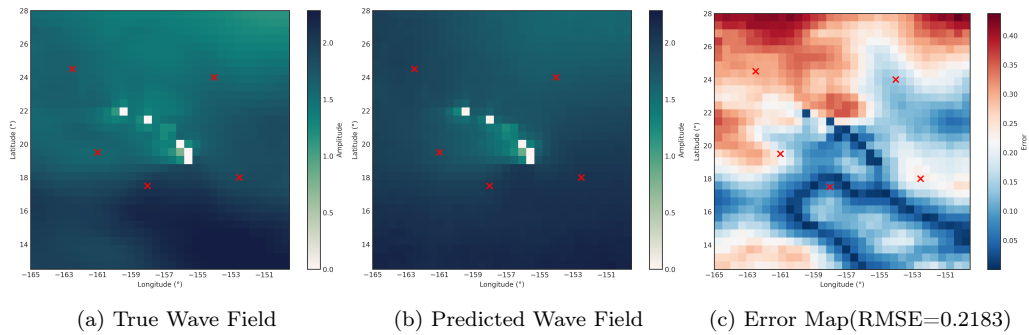


Figure 7: Comparison of true and predicted wave fields for Hawaii dataset (example 4).

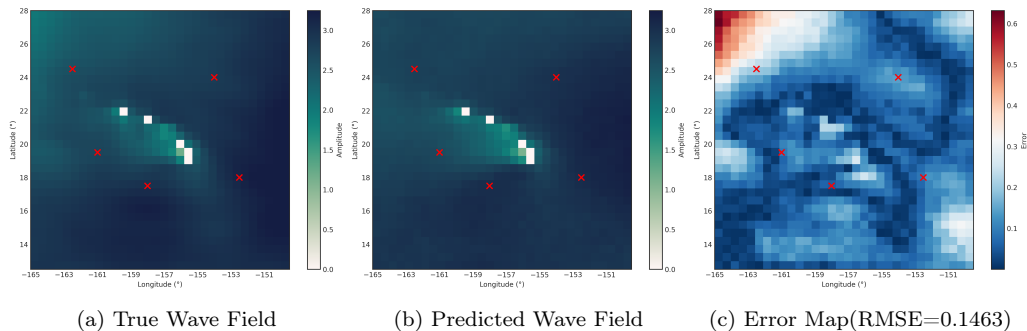


Figure 8: Comparison of true and predicted wave fields for Hawaii dataset (example 5).

where the model performs well or struggles, providing insights for further improvements.

As shown in Figure 9a, the distribution of RMSE values is predominantly centered around lower error magnitudes. The mean RMSE across all samples is 0.2017, and the median RMSE is 0.1887. The slight right-skewness of the distribution, where the mean is slightly higher than the median, indicates the presence of a tail towards higher RMSE values, representing instances where the model’s reconstruction performance was less optimal. However, the majority of reconstruction instances exhibit relatively low errors, demonstrating the general effectiveness of the models.

Figure 9b presents the spatial distribution of the average RMSE for the Hawaii region. The overall mean RMSE for the spatial domain is consistent with the histogram at 0.2017, with a standard deviation of 0.0594 and a maximum observed RMSE of 0.5051 in localized regions. Spatially, the model generally achieves lower RMSE values (represented by darker blue regions) in proximity to the buoy locations, which serve as direct observation points. This suggests that the model effectively leverages the available sparse data. Conversely, higher RMSE values (lighter blues and occasional red patches) are more prevalent in regions further away from the buoys. These areas, characterized by greater data sparsity, present a larger challenge for accurate reconstruction through interpolation or extrapolation.

3.4. Impact of Buoy Configuration on Reconstruction Accuracy

This section evaluates the performance of the AUWave and RWR models for ocean wave field reconstruction under varying data sparsity, with detailed results presented in Table 2 and Figure 10. The results demonstrate that the

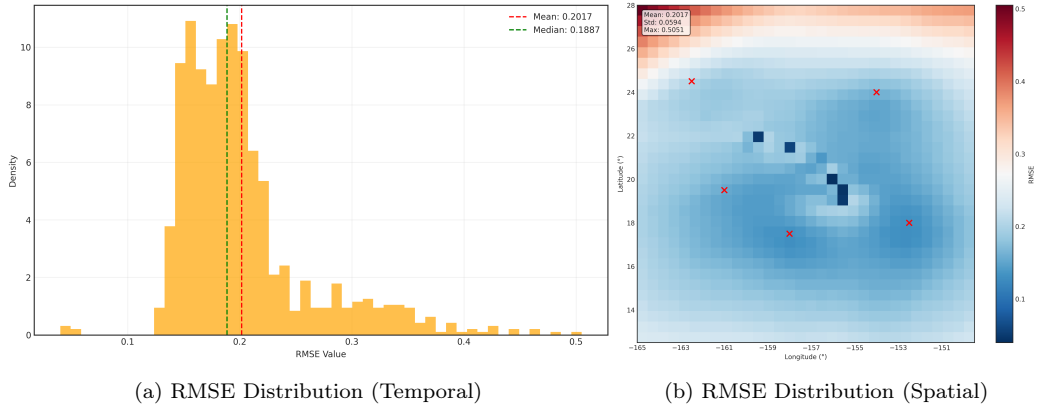


Figure 9: RMSE distribution across the Hawaii dataset. (a) Histogram of RMSE values over all time steps, showing the frequency of different error magnitudes. (b) Spatial distribution of RMSE values at each grid point, with warmer colors indicating higher errors.

AUWave model consistently outperforms the RWR model under data-rich conditions (5 and 4 buoys). In the 5-buoy baseline, for instance, AUWave achieved an RMSE of 0.2129 compared to RWR’s 0.2472. Both models’ performance was sensitive to buoy configuration, with the removal of Buoy 51001 causing the most significant negative impact. Under the extreme sparsity of single-buoy inputs, AUWave maintained its lead in three of the five cases. However, a notable exception occurred when using only Buoy 51002 or 51004, where RWR showed a marginal advantage. These two configurations also corresponded to the highest overall errors for both models.

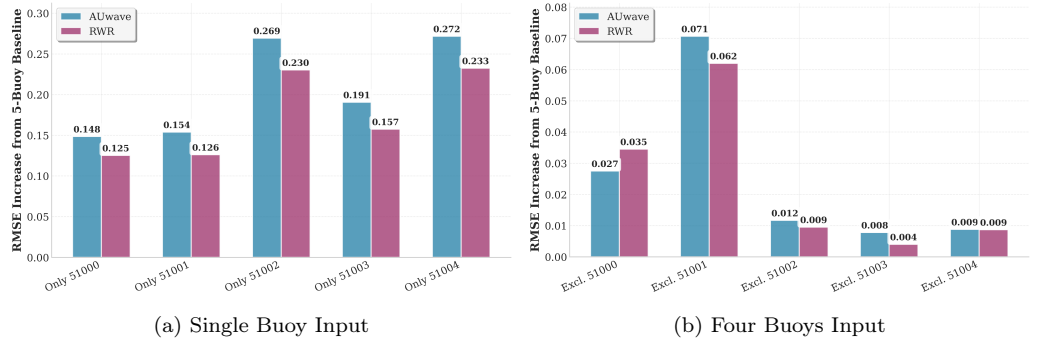


Figure 10: Model Sensitivity to Buoy Configuration.

Buoy Configuration	AUWave	RWR
<i>— Reference Configuration —</i>		
All 5 Buoys (51000, 51001, 51002, 51003, 51004)	0.2129	0.2472
<i>— Removing One Buoy (4-Buoy Combinations) —</i>		
Excluding Buoy 51000	0.2404	0.2817
Excluding Buoy 51001	0.2836	0.3092
Excluding Buoy 51002	0.2246	0.2567
Excluding Buoy 51003	0.2207	0.2512
Excluding Buoy 51004	0.2217	0.2559
<i>— Using Single Buoy (Removing Four Buoys) —</i>		
Buoy 51000 Only	0.3614	0.3724
Buoy 51001 Only	0.3668	0.3732
Buoy 51002 Only	0.4822	0.4774
Buoy 51003 Only	0.4035	0.4046
Buoy 51004 Only	0.4846	0.4797

Table 2: RMSE of Ocean Wave Field Reconstruction Using Different Sparse Buoy Combinations for AUWave and RWR Models

Note: The best (lowest) RMSE value for each configuration is shown in bold.

4. Discussion

4.1. Model performance and error characteristics

This study demonstrates that AUWave can robustly reconstruct 32×32 regional SWH fields from sparse buoy observations. With systematic hyperparameter optimization (Figure 3), the model reached a minimum validation loss of 0.0433. Over the Hawaii test domain, the RMSE distribution is slightly right-skewed, with a mean of 0.2017 and a median of 0.1887 (Figure 9). Case studies (Figures 4-8) show that AUWave reproduces dominant spatial structures. In low-error cases (RMSE ≈ 0.15 - 0.16), predictions closely align with the truth; in the highest-error case (RMSE ≈ 0.36), large-scale patterns persist but local amplitudes deviate systematically. Errors are lowest near buoy locations and increase away from anchors (Figure 9b), reflecting the identifiability limits under sparse sensing. The long tail of the RMSE histogram corresponds to a small fraction of difficult scenes linked to unfavorable sampling geometry, short-term anomalies, or extremes.

4.2. Role of hyperparameters and architecture

Our hyperparameter importance analysis (Figure 3) confirms that training dynamics—particularly the learning rate schedule—remain the dominant factor, which aligns with widely reported findings in neural network optimization. More importantly, architecture-related parameters such as the number of U-Net blocks, layers per block, and base channel width have negligible influence on performance. This suggests that the selected U-Net backbone is already sufficiently expressive for the task and does not require extensive structural modifications.

This result has two key implications. First, it reduces the need for costly architecture search, as most of the performance gains can be achieved through improved optimization strategies rather than redesigning the network. Second, it highlights that our model is robust across a wide range of architectural configurations, making it practical for deployment under varying computational budgets.

4.3. Comparison with the RWR baseline

Architecturally, AUWave differs fundamentally from the RWR baseline in how it fuses sparse information. AUWave decouples temporal/station-wise encoding from hierarchical spatial refinement, using a station-wise MLP to map heterogeneous observations into a spatially aligned latent grid, followed

by a residual U-Net with attention for multi-scale refinement. This design enables recovery of both broad swell patterns and localized gradients, whereas RWR mixes sparse inputs early in a feedforward-CNN stack, imposing a stronger smoothness prior and more homogeneous receptive field growth. While such bias reduces variance under extreme sparsity, it limits detail recovery when more buoys are available.

Empirically, AUWave achieves lower reconstruction errors in richer buoy configurations (e.g., 0.2129 vs. 0.2472 RMSE with five buoys), while RWR shows marginal advantages in some single-buoy cases. The superiority of AUWave can be attributed to several factors: its decoupled fusion improves optimization stability and gradient flow, its multi-scale pathways and bottleneck self-attention preserve high-frequency details while capturing long-range coherence, and its convolutional weight sharing yields better sample efficiency than the larger FC-CNN front-end of RWR. Moreover, the station encoder learns station-specific weights, enhancing robustness to suboptimal buoy layouts and partial station dropout. Finally, AUWave incorporates a physics-aligned inductive bias, as swell propagation requires both non-local coupling and local gradient preservation—properties more naturally captured by an attention-enhanced U-Net than by RWR’s smoother isotropic CNN prior. Nevertheless, RWR retains some relative advantages under extreme sparsity, suggesting that its smoothing bias may provide complementary inductive priors for future hybrid designs.

4.4. *Practical implications*

The results highlight the importance of observational geometry (Table 2, Figure 10). AUWave fuses multi-point observations more effectively than RWR, particularly with 4–5 buoys. However, both models degrade sharply when central anchors are removed; buoy 51001, in particular, proves critical. These findings translate into practical design guidance: prioritize maintenance of key anchors and consider adding or relocating buoys in high-RMSE zones to maximize error reduction per unit cost. AUWave can complement reanalysis and operational forecasting by (1) gap-filling sparse buoy networks, (2) providing high-resolution priors for data assimilation, and (3) enabling emergency reconstructions during outages.

4.5. *Limitations*

This work has several limitations. First, ERA5 is treated as truth, inheriting systematic biases and a 0.5° resolution that may underrepresent mesoscale

and coastal processes. Second, evaluation is limited to Hawaii, whose unique dynamics (e.g., island shielding, swell corridors) may restrict generalization. Third, the objective and metrics emphasize single-time RMSE, without explicit dynamical or spectral consistency. Finally, the framework imposes no hard physical constraints, so non-physical oscillations may occur under extremes.

4.6. Future directions

Future work will:

1. **Incorporate** physics priors (e.g., spectral consistency, PDE-based soft constraints) to mitigate MSE bias.
2. **Adopt** spatiotemporal architectures to capture wave evolution and enable forecasting.
3. **Quantify** uncertainty using Bayesian methods, ensembles, or MC dropout.
4. **Fuse** multimodal inputs (winds, spectra, altimetry, SAR) to strengthen generalization.
5. **Explore** domain adaptation across regions and sea-state regimes.
6. **Couple** active learning with error hotspot maps to guide buoy deployment and close the observation–model loop.

5. Conclusion

In this study, we introduced AUWave, a hybrid deep learning framework designed to reconstruct high-resolution regional wave fields from sparse buoy observations. By integrating a sequence-encoding MLP with a U-Net featuring bottleneck self-attention, AUWave effectively fuses temporal data from individual stations with their broader spatial context. Applied to the Hawaiian region using NDBC and ERA5 data, our optimized model demonstrated robust and accurate performance in reconstructing SWH fields.

The model achieved high-fidelity reconstructions, with errors that were consistently low and stable across the study domain. Our analysis revealed several key findings: (1) Reconstruction accuracy is highest near observation points and degrades predictably with distance, highlighting the inherent limits of sparse sensing. (2) AUWave substantially outperformed a representative baseline method, particularly in configurations with multiple buoys, proving the value of its architecture. (3) The study underscored the critical

influence of buoy placement on overall accuracy, identifying key "anchor" buoys essential for domain-wide performance.

These findings carry significant practical implications. AUWave can serve as a valuable tool to complement existing ocean observation and forecasting systems by: (i) gap-filling data in sparse buoy networks, (ii) providing high-resolution initial fields for data assimilation models, and (iii) enabling rapid reconstruction during satellite or sensor outages. Furthermore, the model's learned error patterns can offer actionable guidance for optimizing the design and maintenance of future ocean observing networks.

This work is primarily limited by its reliance on ERA5 reanalysis as ground truth, its regional focus, and the use of a pixelwise loss function without explicit physical constraints. Future research will aim to incorporate physics-informed learning objectives, develop spatiotemporal models for wave evolution forecasting, quantify reconstruction uncertainty, and fuse multi-modal data such as satellite altimetry and wind fields. Exploring cross-region transfer learning and coupling the model with active learning for guided buoy deployment are also promising directions.

References

- Asch, M., Bocquet, M., Nodet, M., 2016. Data assimilation: methods, algorithms, and applications. SIAM.
- Azman, N.U., Abu Husain, M.K., Mohd Zaki, N.I., Mat Soom, E., Mukhlas, N.A., Syed Ahmad, S.Z.A., 2021. Structural integrity of fixed offshore platforms by incorporating wave-in-deck. *Journal of Marine Science and Engineering* 9, 1027.
- Caloiero, T., Aristodemo, F., Ferraro, D.A., 2022. Annual and seasonal trend detection of significant wave height, energy period and wave power in the mediterranean sea. *Ocean Engineering* 243, 110322. URL: <https://www.sciencedirect.com/science/article/pii/S0029801821016231>, doi:<https://doi.org/10.1016/j.oceaneng.2021.110322>.
- Duan, W., Zhang, L., Cao, D., Sun, X., Zhang, X., Huang, L., 2024. Reconstruction of significant wave height distribution from sparse buoy data by using deep learning. *Coastal Engineering* 194, 104616.
- Fletcher, S.J., 2017. Data assimilation for the geosciences: From theory to application. Elsevier.

- Gaffet, A., Bertin, X., Sous, D., Michaud, H., Roland, A., Cordier, E., 2025. A new global high-resolution wave model for the tropical ocean using wave-watch iii version 7.14. *Geoscientific Model Development* 18, 1929–1946.
- Gao, R., Li, R., Hu, M., Suganthan, P.N., Yuen, K.F., 2023. Dynamic ensemble deep echo state network for significant wave height forecasting. *Applied Energy* 329, 120261. URL: <https://www.sciencedirect.com/science/article/pii/S0306261922015185>, doi:<https://doi.org/10.1016/j.apenergy.2022.120261>.
- Hajinezhadian, M., Behnam, B., 2023. A probabilistic approach to lifetime design of offshore platforms. *Scientific Reports* 13, 7101.
- Han, P., Hildre, H.P., Zhang, H., 2023. Local ocean wave field estimation using a deep generative model of wave buoys. *IEEE Transactions on Geoscience and Remote Sensing* 61, 1–11.
- He, F., Liu, T., Tao, D., 2020. Why resnet works? residuals generalize. *IEEE transactions on neural networks and learning systems* 31, 5349–5362.
- He, K., Zhang, X., Ren, S., Sun, J., 2016. Deep residual learning for image recognition, in: *Proceedings of the IEEE conference on computer vision and pattern recognition*, pp. 770–778.
- Huang, B., Kang, F., Li, X., Zhu, S., 2024. Underwater dam crack image generation based on unsupervised image-to-image translation. *Automation in Construction* 163, 105430.
- Ibarra-Berastegui, G., Sáenz, J., Ulazia, A., Sáenz-Aguirre, A., Esnaola, G., 2023. C mip6 projections for global offshore wind and wave energy production (2015–2100). *Scientific Reports* 13, 18046.
- Ijjeh, A., Ullah, S., Radzienski, M., Kudela, P., 2023. Deep learning super-resolution for the reconstruction of full wavefield of lamb waves. *Mechanical Systems and Signal Processing* 186, 109878.
- Le Traon, P.Y., Dibarboure, G., Lellouche, J.M., Pujol, M.I., Benkiran, M., Drevillon, M., Drillet, Y., Faugère, Y., Remy, E., 2025. Satellite altimetry and operational oceanography: from jason-1 to swot. *Ocean Science* 21, 1329–1347.

- Lv, T., Tao, A., Li, Y.P., Wang, G., Zhu, Y., Zheng, J., 2025. A new framework for selecting observation points and reconstructing wave fields under sparse observations. *Coastal Engineering* , 104836.
- Patra, A., Dodet, G., Min, S.k., Hochet, A., 2024. Quantifying anthropogenic influences on global wave height trend during 1961–2020 with focus on polar ocean. *Geophysical Research Letters* 51, e2023GL106544.
- Ramachandran, P., Zoph, B., Le, Q.V., 2017. Searching for activation functions. arXiv preprint arXiv:1710.05941 .
- Riley, R., 2023. Ndbc wave observation changes, in: *OCEANS 2023 - MTS/IEEE U.S. Gulf Coast*, pp. 1–7. doi:10.23919/OCEANS52994.2023.10337180.
- Riley, R., 2024. Ndbc wave observation system update. *Coastal Engineering Journal* 66, 132–138.
- Seo, H., O’Neill, L.W., Bourassa, M.A., Czaja, A., Drushka, K., Edson, J.B., Fox-Kemper, B., Frenger, I., Gille, S.T., Kirtman, B.P., et al., 2023. Ocean mesoscale and frontal-scale ocean–atmosphere interactions and influence on large-scale climate: A review. *Journal of climate* 36, 1981–2013.
- Shi, J., Su, T., Li, X., Wang, F., Cui, J., Liu, Z., Wang, J., 2023. A machine-learning approach based on attention mechanism for significant wave height forecasting. *Journal of Marine Science and Engineering* 11, 1821.
- Song, C., Alkhalifah, T.A., 2021. Wavefield reconstruction inversion via physics-informed neural networks. *IEEE Transactions on Geoscience and Remote Sensing* 60, 1–12.
- Vaswani, A., Shazeer, N., Parmar, N., Uszkoreit, J., Jones, L., Gomez, A.N., Kaiser, L., Polosukhin, I., 2023. Attention is all you need. URL: <https://arxiv.org/abs/1706.03762>, arXiv:1706.03762.
- Wang, J., Wang, Y., 2022. Evaluation of the era5 significant wave height against ndbc buoy data from 1979 to 2019. *Marine Geodesy* 45, 151–165. URL: <https://doi.org/10.1080/01490419.2021.2011502>, doi:10.1080/01490419.2021.2011502, arXiv:<https://doi.org/10.1080/01490419.2021.2011502>

- Watanabe, S., 2023. Tree-structured parzen estimator: Understanding its algorithm components and their roles for better empirical performance. arXiv preprint arXiv:2304.11127 .
- Wu, L., 2022. Learning a single neuron for non-monotonic activation functions, in: International conference on artificial intelligence and statistics, PMLR. pp. 4178–4197.
- Xu, J., Li, Z., Du, B., Zhang, M., Liu, J., 2020. Reluplex made more practical: Leaky relu, in: 2020 IEEE Symposium on Computers and communications (ISCC), IEEE. pp. 1–7.
- Yao, R., Shao, W., Hu, Y., Xu, H., Zou, Q., 2025. Numeric modeling of sea surface wave using wavewatch-iii and swan during tropical cyclones: An overview. *Journal of Marine Science and Engineering* 13, 1450.
- Zhang, J., Jiang, L., Han, X., Wang, X., 2025. A novel framework for significant wave height prediction based on adaptive feature extraction time-frequency network. *Energy* , 136751.

6. Acknowledgments

The author(s) declare financial support was received for the research, authorship, and/or publication of this article. This research was supported by the Shandong Provincial Lab and Talent Program ("Double Hundred Plan for Overseas Experts" Talent Category, Grant No. WSR2024073 and No. WSR2023026). The authors would like to thank the anonymous reviewers for their valuable feedback and suggestions, which greatly improved the quality of this paper. We also acknowledge the support of the research community and institutions that provided access to the datasets used in this study.

7. Author Contributions

Yilin Zhai was responsible for the overall conceptualization, data analysis, experimental design, and drafting of the manuscript; Hongyuan Shi participated in research discussions, provided valuable guidance and revisions; Chao Zhan reviewed the overall direction of the paper and offered constructive comments; Qing Wang carefully reviewed the manuscript and provided

feedback and suggestions; Zaijin You assisted with data discussions and contributed to several sections of the manuscript; and Ping Dong participated in reviewing and revising the final draft. All authors have read and approved the final version of the manuscript.

8. Conflict of Interest

The authors declare that the research was conducted in the absence of any commercial or financial relationships that could be construed as a potential conflict of interest.